Journal of Building Engineering 98 (2024) 111040

Contents lists available at ScienceDirect

Journal of Building Engineering

journal homepage: www.elsevier.com/locate/jobe

Improving a shell-tube latent heat thermal energy storage unit for building hot water demand using metal foam inserts at a constant pumping power

Fathi Alimi [a], Hakim S. Sultan Aljibori [b], Mohamed Bouzidi [c,d], Aeshah Alasmari [e], Shima Yazdani [f], Mehdi Ghalambaz [g,*]

[a] Department of Chemistry, College of Science, University of Ha'il, P.O. Box 2440, Ha'il, 81441, Saudi Arabia
[b] College of Engineering, University of Warith Al-Anbiyaa, Karbala, 56001, Iraq
[c] Department of Physics, College of Science, University of Ha'il, P.O. Box 2440, Ha'il, Saudi Arabia
[d] Laboratoire de Recherche sur les Hétéro-Epitaxies et Applications, Faculty of Science of Monastir, University of Monastir, Monastir, 5019, Tunisia
[e] Department of Physics, College of Science, University of Bisha, Bisha, 61922, Saudi Arabia
[f] Laboratory on Convective Heat and Mass Transfer, Tomsk State University, 634050, Tomsk, Russia
[g] Department of Mathematics, Saveetha School of Engineering, SIMATS, Chennai, India

ARTICLE INFO

Keywords:
Heat transfer enhancement
Melting and solidification
Energy storage power
Metal foam inserts in heat transfer liquid

ABSTRACT

The phase transition heat transfer during the melting and solidification processes of phase change materials (PCMs) was modeled in a shell-tube thermal energy storage unit. For the first time, special attention was dedicated to the heat transfer enhancement on the heat transfer fluid (HTF) side by placing metal foam (MF) inserts in the HTF tube. The MF inserts on the HTF side were placed next to the fin bases to produce the maximum heat transfer enhancement. A two-temperature local thermal non-equilibrium model was applied to accurately model the transient heat transfer in the MF domains. To perform a fair heat transfer analysis and consider the hydrodynamic aspects of heat transfer, the pumping power for driving the HTF fluid was kept fixed. The finite element method with automatic time-step control was used to integrate the model equations. Results show that the insertion of the MF in the HTF tube enhances conduction heat transfer but reduces flow for a constant pump power. Using a small amount of MF provides a good flow rate and a convective heat transfer while using a large amount of MF provides good conduction heat transfer but a poor flow rate and convection. A moderate amount of MF inserts results in poor conduction and a poor flow rate, notably increasing the phase transition time. A 5 % MF insert could provide about a 13 % shorter solidification time compared to a 25 % MF insert. Thus, a well-designed and engineered MF insert configuration on the HTF side can reduce the phase transition time and improve the energy storage power.

1. Introduction

Thermal energy storage is vitally important in renewable energy systems. Its primary function is to mitigate the discrepancies between the availability of energy and its consumption, especially critical with intermittent renewable sources like solar and wind. By implementing demand response programs within microgrids, adjustments to electricity usage can be made about fluctuating

* Corresponding author.
E-mail addresses: alimi.fathi@gmail.com (F. Alimi), hakim.s@uowa.edu.iq (H.S.S. Aljibori), elbouzidimed16@yahoo.com (M. Bouzidi), aymalasmari@ub.edu.sa (A. Alasmari), shima.yazdaani@gmail.com (S. Yazdani), ghalambaz.mehdi@gmail.com (M. Ghalambaz).

https://doi.org/10.1016/j.jobe.2024.111040
Received 28 July 2024; Received in revised form 6 October 2024; Accepted 11 October 2024
Available online 11 October 2024

availability and pricing of power. Such adaptations are facilitated effectively through the deployment of thermal energy storage units [1].

Latent heat thermal energy storage (LHTES) is a particularly effective method of storing and releasing heat which has found many applications in solar heating [2,3] and photovoltaic systems [4]. LHTES units utilize phase change materials (PCMs) that absorb and release heat during phase transitions, thereby storing energy [5]. LHTES systems are crucial for improving the efficiency and sustainability of thermal management in buildings, particularly through the integration of solar energy. However, LHTES systems often suffer from low thermal conductivity and leakage problems, resulting in a low heat storage and release rate [6]. Gao et al. [7] noted that while LHTES using paraffin provides greater storage within the phase-change temperature range, challenges in fully solidifying the paraffin limit its effective capacity, underscoring the need for optimization. Saxena et al. [8] enhanced solar air heaters with small, cost-effective PCM containers using materials like coconut oil and paraffin wax, which proved particularly effective in mild cold climates by extending heating durations and improving thermal performance. Almitani et al. [9] improved phase change rates by integrating multi-walled carbon nanotubes (MWCNTs) into PCMs, speeding up the melting process by up to 3.86 % and optimizing LHTES for rapid thermal response. Additionally, Jin et al. [10] demonstrated that integrating LHTES with solar-assisted heat pumps could cut energy consumption by 56.6 %, significantly lowering operational costs and enhancing renewable energy use in heating. Wu et al. [11] further showed that incorporating PCMs into the structures of buildings, such as in ventilated walls for passive solar heating, can effectively dampen indoor temperature fluctuations, providing a more stable and comfortable environment.

To address poor heat transfer issues, one solution is the integration of porous supports and PCMs to fabricate shape-stabilized phase change materials (ss-PCMs) [12]. Shell-and-tube LHTES units are a common design, and geometric and operational parameters can significantly influence their performance [13]. For instance, the ratio of the shell-to-tube radius and the heat transfer fluid (HTF) flow rate and temperature can all impact the charging time and stored energy in the LHTES systems [14]. Notably, techniques such as fins, encapsulation, and porous media stand out as key methods for enhancing the heat transfer efficiency of solar water heating systems [15].

A range of techniques to enhance heat transfer have been designed to boost the efficiency of phase change materials. These techniques include the use of extended surfaces [16] and fins [17,18], nanoparticles and nano-additives [19,20], and metal foams [21,22]. The utilization of metal foams in shell-and-tube LHTES systems significantly enhances heat transfer due to their high surface area and superior thermal conductivity [25]. Likewise, the strategic design of fins, when integrated into these units, substantially improves heat transfer via natural convection. This improvement is credited to the specific engineering of fins to optimize their design features [23,24]. Fins have long been used to enhance the heat transfer rate in energy systems. Considering their application in LHTES units, several excellent research studies have addressed their effectiveness in improving the energy storage/release rate in LHTES systems. As explored in Ref. [26], the arrangement of H-type fins emphasizes that even geometric variations such as fin width and the curvy angles of circular layers can markedly influence the melting behavior, with optimal configurations reducing melting time significantly.

An innovative approach to enhancing heat transfer in shell-and-tube LHTES units is the incorporation of high-conductivity fins [27]. The optimization of these fin designs can be achieved through methods such as topology optimization combined with multi-phase computational fluid dynamics, enabling the development of more effective and complex geometries. Studies have demonstrated that natural convection can significantly boost both melting and solidification processes when fins are carefully designed with specific features [27]. Another research effort investigated the impact of varying fin distributions on the discharge performance of shell-and-tube LHTES units, revealing that fin placement plays a crucial role in influencing energy storage efficiency [28]. Using a twisted elliptical inner tube with a 720° twist and 11 fins has increased melting efficiency by over 156 % and reduced heat loss by more than 41 % [29].

Incorporating fins into LHTES systems has markedly improved heat transfer rates and overall thermal efficiency. Structurally optimized spiral fins, adjusting thickness, height, and spacing, significantly reduce the complete melting time of PCMs by 15.01 %, thanks to better convective and conductive heating processes [30]. Additionally, the adoption of staggered fin-foam synergistic configurations cuts down full melting times by 58.67 %, with an additional 13.18 % reduction achieved by dividing the system into four segments [31]. Research into H-type fins reveals that broader fins significantly boost melting rates by 88 % and 32 % over narrower options, while adjustable curvy fin angles modify energy storage and melting effectiveness [26].

LHTES systems are crucial for enhancing energy storage efficiency in buildings, especially with renewable energy like solar. Wang et al. [32] demonstrated that a novel shell-and-tube LHTES unit with a high-endothermic film and PCMs significantly boosts thermal performance, increasing average indoor temperatures by up to 2.6 °C and reducing fluctuations by 2.7 °C, while cutting electricity use by 33.3 % at night. Şimşek and Demirci [33] found that adding fins to heat exchangers reduced PCM melting times by up to 86.33 %, enhancing LHTES system efficiency [3]. Twisted fins in horizontal double-tube heat exchangers create a swirling flow, reducing thermal resistance and improving charge and discharge rates by 10–14 % over straight fins and up to 40 % compared to finless configurations [34].

Some studies utilized metal foams to improve the heat transfer and response time of LHTES systems. A compact LHTES unit attached to domestic radiators can save energy and reduce CO_2 emissions. An aluminum foam embedded in PCM enhances heat storage/retrieval. The metal foam-enhanced unit maintains a constant temperature of 54 °C during discharge. A higher metal foam porosity leads to shorter charging/discharging times, with 97 % porosity being desirable [35]. Compared to traditional methods, introducing graded metal foams and mechanical rotation improved the total melting time by up to 42.42 %. The strategic use of anisotropic metal foams in LHTES systems notably boosts heat transfer and energy storage efficiency. Ghalambaz et al. [36] revealed that these foams, tailored for optimal thermal conductivity and permeability, dramatically improve the phase transition and charging times of LHTES units. An optimal tilt and anisotropic angle configuration can cut charging times by up to 20 % without compromising the unit's weight or capacity, showcasing the potential for more efficient energy storage solutions. Shen et al. [37] improved cascaded LHTES systems by embedding

PCMs with tuned porosity, increasing heat storage rates by 73.21 % and reducing overcharging by up to 89.66 %.

Several recent studies utilized combined approaches to enhance the response time of LHTES systems. Wołoszyn and Szopa [38] addressed the low thermal conductivity issue in LHTES systems by proposing a helical-coiled shell-and-tube unit with spiral fins. The design combines the benefits of horizontal and vertical systems, offering improved energy and exergy efficiency, as well as reduced PCM melting and solidification times. Numerical experiments compared nine thermal energy storage designs, revealing that the proposed unit outperforms vertical and horizontal shell geometries with significant reductions in melting and solidification times (up to 60 % and 26 % reduction, respectively). The proposed design achieves superior overall exergy efficiency while demonstrating efficient solidification and melting times. In contrast, conical shell geometries effectively reduce melting time but lead to an increase in total solidification duration. Guo et al. [39] conducted experiments to evaluate the role of metal fins and foam in enhancing heat transfer of phase change materials. They introduced a new hybrid fin-foam tube and compared it with bare, fin-only, and metal foam tubes. Thermal performance was assessed based on parameters like melting duration, temperature response, and uniformity. Results revealed that the hybrid fin-foam structure was the most effective, reducing complete melting time by 83.35 % and enhancing temperature response by 529.1 %. While metal foam contributed to better temperature uniformity, fins reduced it. Therefore, metal foams are recommended when uniform temperature distribution is the primary concern.

Extensive literature demonstrates the potential of metal foams, fins, or their combination to enhance energy storage and release rates in LHTES systems. However, little attention has been paid to the improvement of heat transfer between the HTF and PCM sides. The current research pioneers the investigation of inserting metal foams adjacent to the fin basis within a heat transfer tube to amplify heat transfer rates locally. The objective is to improve the heat transfer between the working fluid and PCM domain, resulting in enhanced response time for the energy storage system.

2. Physical model

2.1. Model description

Integrating LHTES systems with renewable energy sources enhances their efficiency and reliability, particularly in solar thermal applications. By leveraging the LHTES unit's ability to mitigate energy variability, solar thermal systems can provide a more consistent and reliable heat supply, which is essential for expanding the use of solar energy in residential and commercial heating.

The schematic view of the concentrated solar heating setup for building heating underscores the role of LHTES in advancing solar energy technologies. Solar energy's reliance on variable weather conditions and time makes it intermittent by nature. An LHTES system can store substantial energy at phase transition temperatures in a compact space, thus stabilizing the energy output in transient solar systems. This system includes a hot water storage tank, solar collector, an LHTES unit, and circulation pumps. Solar heat is absorbed by water heated through the solar collector in the form of sensible heat, and this heated water is then stored in a tank, prepared to stream hot water as needed.

Additionally, an auxiliary loop connects the hot water tank to the LHTES unit. This occurs during periods of surplus energy production or low energy demand. The auxiliary pump is engaged to shift excess heat to the LHTES unit. In contrast, when solar energy supply falls short, the tank retrieves energy from the LHTES unit. Fig. 1 displays a schematic of this system, featuring a vertically oriented shell tube with the HTF entering from the bottom.

Fig. 2 illustrates the design of a shell-tube shape LHTES unit. Here, the HTF, water, flows into the tube at a pressure of P_{in} and exits from the upper outlet at zero pressure. The tube's walls are made of copper with a specific thickness t_{wall} and an outer radius of R. Inside the tube shell, a copper-based uniform metal foam layer exists, surrounded by a shell filled with a composite of the same metal foam and PCM. Metal fins are integrated to boost heat exchange between the HTF and the PCM domain, which is thoroughly infused with paraffin wax. This wax undergoes a phase change, storing and releasing latent heat at a transition temperature T_f. During the system's operation in either discharging or charging mode, heat is transferred through the tube wall between the water and the paraffin wax

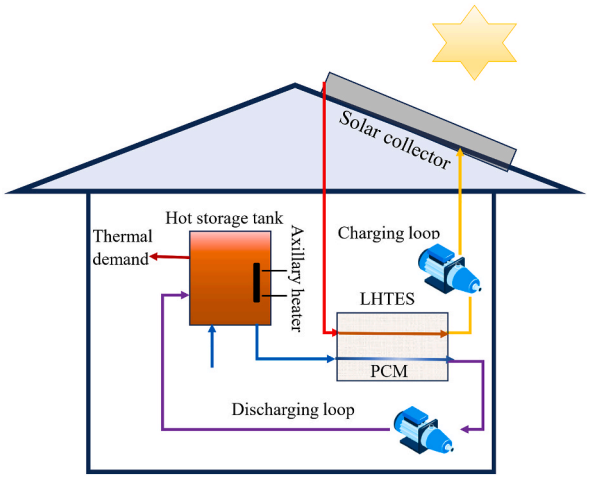

Fig. 1. Illustration of a schematic diagram depicting a hybrid electric heating solar system incorporating an LHTES unit. The heat storage tank holds on-demand heated water, and the LHTES unit provides additional heat storage capacity.

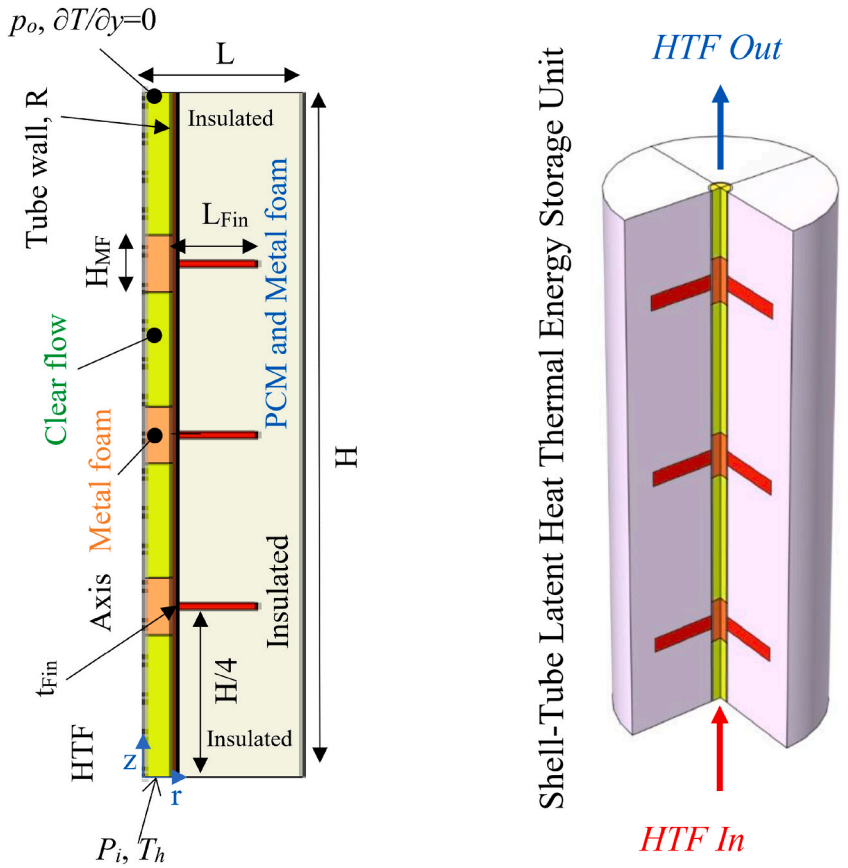

Fig. 2. Schematic view of LHTES unit and physical model. The metal foams are placed in the tube and inside the shell to support heat transfer at both the HTF and the shell side.

PCM, resulting in a change in the outlet water temperature.

The main objective is to investigate the heat transfer dynamics within the LHTES unit, particularly by examining the three distinct layers of metal foam inserts. The heat transfer in this system is divided into two primary sections: the HTF path and the PCM storage area. An isotropic metal foam layer has been incorporated into the HTF tube to enhance heat transfer efficiency and decrease the duration needed for thermal storage.

The volume of MF insert to the total volume of the HTF tube was introduced as the volume ratio of MF ($0.05<VR_{MF}<0.7$). $Th = T_f$

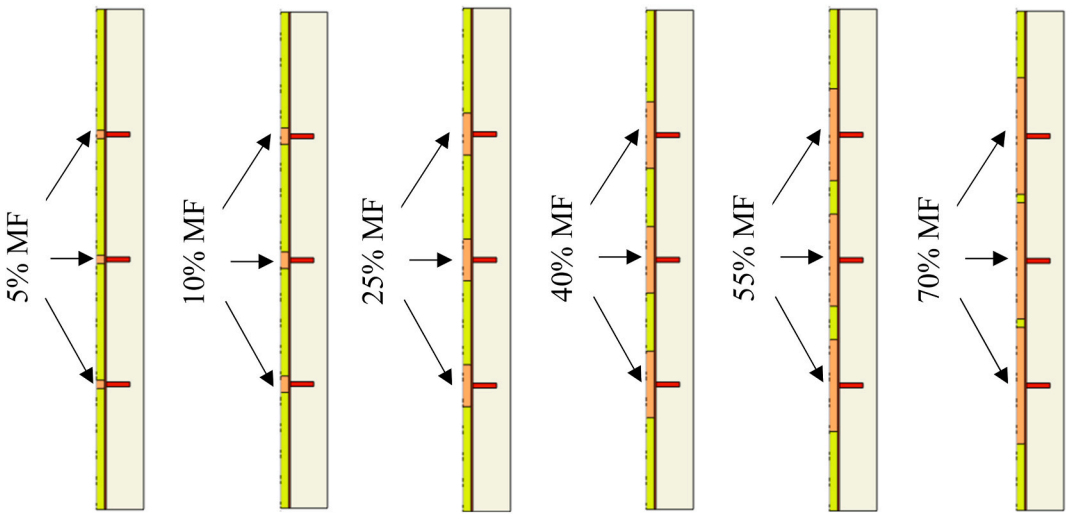

Fig. 3. An overview of metal foam (MF) inserts in a heat transfer fluid (HTF) tube, showing configurations with varying total percentages of MF inserts. The tube is filled with 5 %, 10 %, 25 %, 40 %, 55 %, and 70 % MF inserts by volume.

+ 15 °C and $Tc = T_f$ - 15 °C are considered as the operating temperatures of the energy storage system. Fig. 3 shows the model with various amounts of MF inserts on the HTF side. The volume ratio of the MF insert is introduced as follows:

$$VR_{MF}=V_{MF}/V_{HTF} = 3 \times H_{MF}/H \quad (1)$$

where V_{MF} is the total volume of MF inserted in the HTF tube, and V_{HTF} is the total tube volume.

2.2. Mathematical equations

The governing equations in this study encompass fluid flow in both clear and porous domains, specifically for the HTF side. Moreover, to analyze heat transfer within the metal foam (MF) inserts, a two-equation local thermal non-equilibrium (LTNE) model is utilized. For the PCM-MF side, the governing equations involve fluid flow with buoyancy effects within the porous domain.

Table 1
The principal equations in model regions.

Region	Equation name	Equation formula	Eq.
HTF - Clear	Continuity	$\frac{1}{r}\frac{\partial(ru_r)}{\partial r}+\frac{\partial u_z}{\partial z}=0$	(2)
	r-Momentum	$\rho_{HTF}\left(\frac{\partial u_r}{\partial t}+u_z\frac{\partial u_r}{\partial z}+u_r\frac{\partial u_r}{\partial r}\right)=-\frac{\partial p}{\partial r}+\frac{\mu_{HTF}}{r}\frac{\partial}{\partial r}\left(r\frac{\partial u_r}{\partial r}\right)+\mu_{HTF}\frac{\partial^2 u_r}{\partial z^2}-\frac{\mu_{HTF}u_r}{r^2}$	(3)
	z-Momentum	$\rho_{HTF}\left(\frac{\partial u_z}{\partial t}+u_z\frac{\partial u_z}{\partial z}+u_r\frac{\partial u_z}{\partial r}\right)=-\frac{\partial p}{\partial z}+\frac{\mu_{HTF}}{r}\frac{\partial}{\partial r}\left(r\frac{\partial u_z}{\partial r}\right)+\mu_{HTF}\frac{\partial^2 u_z}{\partial z^2}$	(4)
	Energy	$(\rho C_p)_{HTF}\left(\frac{\partial T}{\partial t}+u_z\frac{\partial T}{\partial z}+u_r\frac{\partial T}{\partial r}\right)=k_{HTF}\left(\frac{1}{r}\frac{\partial}{\partial r}\left(r\frac{\partial T}{\partial r}\right)+\frac{\partial^2 T}{\partial z^2}\right)$	(5)
HTF - MF	Continuity	$\frac{1}{r}\frac{\partial(ru_r)}{\partial r}+\frac{\partial u_z}{\partial z}=0$	(6)
	r-Momentum	$\frac{\rho_{HTF}}{\varepsilon}\frac{\partial u_r}{\partial t}+\frac{\rho_{HTF}}{\varepsilon^2}\left(u_z\frac{\partial u_r}{\partial z}+u_r\frac{\partial u_r}{\partial r}\right)=-\frac{\partial p}{\partial r}+\frac{\mu_{HTF}}{\varepsilon}\left[\frac{1}{r}\frac{\partial}{\partial r}\left(r\frac{\partial u_r}{\partial r}\right)-\frac{u_r}{r^2}+\frac{\partial^2 u_r}{\partial z^2}\right]-\rho_{HTF}\frac{C_F}{\sqrt{\kappa}}|u|u_r-\frac{\mu_{HTF}}{\kappa}u_r$	(7)
	z-Momentum	$\frac{\rho_{HTF}}{\varepsilon}\frac{\partial u_z}{\partial t}+\frac{\rho_{HTF}}{\varepsilon^2}\left(u_z\frac{\partial u_z}{\partial z}+u_r\frac{\partial u_z}{\partial r}\right)=-\frac{\partial p}{\partial z}+\frac{\mu_{HTF}}{\varepsilon}\left[\frac{\partial^2 u_z}{\partial z^2}+\frac{1}{r}\frac{\partial}{\partial r}\left(r\frac{\partial u_z}{\partial z}\right)\right]-\rho_{HTF}\frac{C_F}{\sqrt{\kappa}}|u|u_z-\frac{\mu_{HTF}}{\kappa}u_z$	(8)
	Fluid-Energy	$(\rho C_p)_{HTF}\left(\varepsilon\frac{\partial T_{HTF}}{\partial t}+\left(u_z\frac{\partial T_{HTF}}{\partial z}+u_r\frac{\partial T_{HTF}}{\partial r}\right)\right)=\frac{1}{r}\frac{\partial}{\partial r}\left(k_{eff,HTF}r\frac{\partial T_{HTF}}{\partial r}\right)+\frac{\partial}{\partial z}\left(k_{eff,HTF}\frac{\partial T_{HTF}}{\partial z}\right)+h_{sf}A_{sf}(T_{MF}-T_{HTF})$	(9)
	MF-Energy	$(\rho C_p)_{MF}(1-\varepsilon)\frac{\partial T_{MF}}{\partial t}=\frac{1}{r}\frac{\partial}{\partial r}\left(k_{eff,MF}r\frac{\partial T_{MF}}{\partial r}\right)+\frac{\partial}{\partial z}\left(k_{eff,MF}\frac{\partial T_{MF}}{\partial z}\right)+h_{sf}A_{sf}(T_{HTF}-T_{MF})$	(10)
Tube wall	Energy	$(\rho C_p)_{Wall}\frac{\partial T}{\partial t}=k_{Wall}\left(\frac{\partial^2 T}{\partial z^2}+\frac{1}{r}\frac{\partial}{\partial r}\left(r\frac{\partial T}{\partial r}\right)\right)$	(15)
PCM - MF	Continuity	$\frac{1}{r}\frac{\partial(ru_r)}{\partial r}+\frac{\partial u_z}{\partial z}=0$	(16)
	r-Momentum	$\frac{\rho_{PCM}}{\varepsilon}\left(\frac{\partial u_r}{\partial t}+\frac{1}{\varepsilon}\left(u_z\frac{\partial u_r}{\partial z}+u_r\frac{\partial u_r}{\partial r}\right)\right)=-\frac{\partial p}{\partial r}+A_{mush}\frac{(1-\varphi(T))^2}{\lambda_{mush}+\varphi^3(T)}u_r+$	(17)
	z-Momentum	$\frac{\rho_{PCM}}{\varepsilon}\left(\frac{\partial u_z}{\partial t}+\frac{1}{\varepsilon}\left(u_z\frac{\partial u_z}{\partial z}+u_r\frac{\partial u_z}{\partial r}\right)\right)=-\frac{\partial p}{\partial z}+A_{mush}\frac{(1-\varphi(T))^2}{\lambda_{mush}+\varphi^3(T)}u_z+\frac{\mu_{PCM}}{\varepsilon}\left[\frac{\partial^2 u_z}{\partial z^2}+\frac{1}{r}\frac{\partial}{\partial r}\left(r\frac{\partial u_z}{\partial z}\right)\right]-\rho_{PCM}\frac{C_F}{\sqrt{\kappa}}|u|u_z-\frac{\mu_{PCM}}{\kappa}u_z+g\rho_{PCM}\beta_{PCM}(T-T_0)$	(18)
	Fluid-Energy	$(\rho C_p)_{PCM}\left(\varepsilon\frac{\partial T_{PCM}}{\partial t}+\left(u_z\frac{\partial T_{PCM}}{\partial z}+u_r\frac{\partial T_{PCM}}{\partial r}\right)\right)=\frac{1}{r}\frac{\partial}{\partial r}\left(k_{eff,PCM}r\frac{\partial T_{PCM}}{\partial r}\right)+\frac{\partial}{\partial z}\left(k_{eff,PCM}\frac{\partial T_{PCM}}{\partial z}\right)-\varepsilon\rho_{PCM}L_{PCM}\frac{\partial f(T)}{\partial t}+h_v(T_{MF}-T_{PCM})$	(19)

(continued on next page)

Table 1 (*continued*)

Region	Equation name	Equation formula	Eq.
	MF-Energy	$(\rho C_p)_{MF}(1-\varepsilon)\frac{\partial T_{MF}}{\partial t} = \frac{1}{r}\frac{\partial}{\partial r}\left(k_{eff,MF} r \frac{\partial T_{MF}}{\partial r}\right) + \frac{\partial}{\partial z}\left(k_{eff,MF}\frac{\partial T_{MF}}{\partial z}\right) + h_v(T_{PCM} - T_{MF})$	(20)
Molten field	Liquid field	$f(T) = \begin{cases} 0 & T < \left(T_f - \frac{1}{2}\Delta T_f\right) \\ \frac{1}{2} + \frac{(T-T_f)}{\Delta T_f} & \left(T_f - \frac{1}{2}\Delta T_f\right) \le T \le \left(T_f + \frac{1}{2}\Delta T\right)_f \\ 1 & T > \left(T_f + \frac{1}{2}\Delta T_f\right) \end{cases}$	(21)

Table 2
Relationships for the thermophysical properties.

Property	Notation	Formula	No.
Effective thermal conductivity of MF in MFL [41,42]	$k_{eff,MF}$	$k_{eff,MF} = \frac{(1-\varepsilon)}{3} k_{MF,PCM}$	(22)
Effective thermal conductivity of PCM in MFL [41,42]	$k_{eff,MF}$	$k_{eff,PCM} = k_{PCM}\frac{\varepsilon+2}{3}$	(23)
Permeability [41,42]	κ	$\kappa = \frac{\varepsilon^2}{36}\frac{\left(\sqrt{\frac{\kappa_{tor}}{3\varepsilon}} d_{fp}\right)^2}{\kappa_{tor}(\kappa_{tor}-1)}$	(24)
Pore diameter [43]	d_{fp}	$d_{fp} = 2.54 \times 10^{-2}/PPI$	(25)
Pore characteristics [43]	d_{fs}	$d_{fs} = 1.18\left\{\frac{1}{1-e^{\frac{(\varepsilon-1)}{0.04}}}\right\}\sqrt{\frac{(1-\varepsilon)}{3\pi}} d_{fp}$	(26)
Pore flow Tortuosity [43]	κ_{tor}	$\frac{1}{\kappa_{tor}} = \frac{1}{\varepsilon}\left[\frac{3}{4} + \frac{\sqrt{9-8\varepsilon}}{2}\times \cos\left\{\frac{4}{3}\pi + \frac{1}{3}\cos^{-1}\left(\frac{8\varepsilon^2+27-36\varepsilon}{(9-8\varepsilon)^{\frac{3}{2}}}\right)\right\}\right] d_{fp}$	(27)
Frochheimer coefficient [43]	C_F	$C_F = 0.00212 \times \left(\frac{d_{fs}}{d_{fp}}\right)^{-1.63} (1-\varepsilon)^{-0.132}$	(28)
interface heat transfer in volumetric form between MF and PCM in MFL [44]	h_v	$h_v = \frac{k_{PCM}}{d_{fs}^2} Nu_v$	(29)
Nusselt number in MFL [44]	Nu_v	$Nu_v = \begin{cases} \left(76.99 - 152.01 \times \varepsilon + 75.04 \times \varepsilon^2\right), 0 \le \mathrm{Re} \le 0.1 \\ \left(1.72 + 1.71 \times \varepsilon - 3.46 \times \varepsilon^2\right) \times \mathrm{Re}^{0.26} \times \mathrm{Pr}^{0.28}, 0.1 < \mathrm{Re} \le 1 \end{cases}$	(30)
HTF Nusselt number in MF insert [45,46]	Nu_{sf}	$Nu_{sf} = \begin{cases} 0.76\,\mathrm{Pr}^{0.37}\mathrm{Re}_{MF}^{0.4}, 1 \le \mathrm{Re}_{MF} \le 40 \\ 0.52\,\mathrm{Pr}^{0.37}\mathrm{Re}_{MF}^{0.5}, 40 \le \mathrm{Re}_{MF} \le 1000 \\ 0.26\,\mathrm{Pr}^{0.37}\mathrm{Re}_{MF}^{0.6}, 1000 \le \mathrm{Re}_{MF} \le 10^5 \end{cases}$	(31)
MF insert's interface heat transfer between HTF and MF	h_{sf}	$h_{sf} = Nu_{sf} \times k_{sf}/d_{fp}$	(32)
Pore scale Reynolds number in MF insert	Re_{MF}	$Re_{MF} = \rho_{HTF} \times d_{sp} \lvert u \rvert / (\varepsilon \times \mu_{HTF})$	(33)
MFL's Pore scale Reynolds number	Re	$Re = d_{fs} \times u_{PCM} \times \rho_{PCM}/\mu_{PCM}$	(34)
Pore-scale Reynolds number in MFL	Re	$Re = d_{fs} \times u_{PCM} \times \rho_{PCM}/\mu_{PCM}$	(35)
Prandtl number in MFL	Pr	$Pr = \mu_{PCM} \times \rho_{PCM}/\alpha_{PCM}$	(36)
Thermal diffusivity in MFL	α_{PCM}	$\alpha_{PCM} = k_{PCM}/(\rho C_p)_{PCM}$	(37)
Thermal diffusivity in MF insert	α_{HTF}	$\alpha_{HTF} = k_{HTF}/(\rho C_p)_{HTF}$	(38)

(*continued on next page*)

Table 2 (*continued*)

Property	Notation	Formula	No.
Prandtl number in MF insert	Pr	$Pr = \mu_{PCM} \times \rho_{PCM}/\alpha_{PCM}$	(39)
Interface surface between HTF and MF pore [44–47]	A_{sf}	$A_{sf} = \frac{3\pi\left(1 - e^{-\frac{(1-\varepsilon)}{0.004}}\right) d_{fs}}{0.59 d_{fp}}$	(40)
Heat capacity of PCM	$(\rho C_p)_{PCM}$	$(\rho C_p)_{PCM} = f(\rho C_p)_s + (1-f)(\rho C_p)_l$	(41)
Density of PCM	ρ_{PCM}	$\rho_{PCM} = f\rho_s + (1-f)\rho_l$	(42)

Table 3
The thermophysical characteristics of the utilized material.

Materials	ρ (kg/m^3)	k (W/m.K)	C_p (J/kg.K)	L (kJ/kg)	T_m (°C)	μ (kg/m.s)	β (1/K)
Paraffin (solid/liquid) [50–52]	916/790	0.21/0.12	2700/2900	176	49–54	0.0036	0.00091
Water [53]	997.1	0.613	4179	–	–	0.000957	0.00021
Copper foam [54]	8900	380	386	–	–	–	–

An LTNE heat equation incorporating phase change in the fluid phase is also utilized [40]. The thermal behavior of the fins is accounted for through the inclusion of conjugate solid conduction heat transfer. Table 1 summarizes the governing equations to provide a comprehensive overview, and Table 2 provides closure models for the fluid and porous matrix phases.

In the HTF domain, the effective thermal conductivity of HTF and MF [41,42,45,48] can be obtained using:

$$k_{eff} = \frac{\sqrt{2}}{2(M_A + M_B + M_C + M_D)} \tag{43}$$

$$M_A = \frac{4\sigma}{((2e^2 + \pi\kappa(1-e))k_{MF} + (4 - 2e^2 - \pi\sigma(1-e))k_{HTF})} \tag{44}$$

$$M_B = \frac{(\varepsilon - 2\sigma)^2}{((e-2\sigma)e^2 k_{MF} + (2e - 4\sigma - e^2(e-2\sigma))k_{HTF})} \tag{45}$$

$$M_C = \frac{\left(\sqrt{2} - 2\sigma\right)^2}{\left(2\pi\sigma^2\left(1 - 2\sqrt{2}\ e\right)k_{MF} + 2\left(\sqrt{2} - 2e - \pi\sigma^2\left(1 - 2\sqrt{2}\ e\right)\right)k_{HTF}\right)} \tag{46}$$

$$M_D = \frac{2e}{(e^2 k_{MF} + (4 - e^2)k_{HTF})} \tag{47}$$

$$\sigma = \sqrt{\frac{\sqrt{2}\left(2 - \frac{5}{8}\sqrt{2}\,e^3 - 2\varepsilon\right)}{\left(\pi\left(3 - 4\sqrt{2}\,e - e\right)\right)}} \tag{48}$$

$$\sigma = \sqrt{\frac{\sqrt{2}\left(2 - \frac{5}{8}\sqrt{2}\ e^3 - 2\varepsilon\right)}{\left(\pi\left(3 - 4\sqrt{2}\ e - e\right)\right)}}, e = 0.339 \tag{49}$$

To compute $k_{\text{eff,MF}}$, input a value of zero for k_{HTF}. Conversely, to determine $k_{\text{eff,HTF}}$, set k_{MF} to zero. Furthermore, to improve the stability of the solver and facilitate model convergence, the dynamic PCM viscosity is intentionally modified. An equation has been offered to express this: $\mu_{\text{PCM}} = f\,\mu_{\text{PCM,l}} + (1\text{-}f) \times \mu_{\infty}$, where μ_{∞} stands for a remarkably elevated viscosity value of 10^4 Pa s. With this approach, we ensure that the viscosity aligns with the typical dynamic viscosity $\mu_{\text{PCM,l}}$ in the liquid state (where $f = 1$). Simultaneously, it artificially inflates considerably in the solid state (where $f = 0$). This artificial augmentation of dynamic viscosity is crucial in achieving the main goal of the source terms: imposing zero velocities in solid regions. Not only does this specific definition of dynamic viscosity boost solver stability and smoothen simulations, but it also upholds the authenticity of the physical model. Table 3 lists the thermophysical properties of utilized materials.

2.3. Model boundary and initial conditions

The whole domain is initially subjected to a significantly low (for melting) or high (for solidification) temperature, T_0. Then, a heated/cooled HTF liquid with a temperature *Tin* is poured into the tube, causing the PCM within the shell to melt/solidify. Hence, the initial condition is set as $T = T_0$. At the interfaces, the boundary conditions manifest as temperature and heat continuity.

The heat flux is split into two pathways for the interfaces of the MF (inside the LTNE model) and the tube wall. The first pathway,

represented by $q_{PCM} \times \varepsilon$ or $q_{HTF} \times \varepsilon$, is linked to the unoccupied space. The second pathway relates to heat transmission through the solid matrix, and it correlates with the solid volume (1-ε). This pathway can be denoted by $q_{MF} \times \varepsilon$. Hence, the interface boundary condition can be articulated as per reference [49]:

$$q_{Wall} = q_{PCM}\varepsilon + q_{MF}(1-\varepsilon) \tag{50}$$

The HTF fluid is subjected to an outflow with zero-gauge discharge pressure, while the inlet is maintained at an inlet pressure P_{in}, and a steady temperature of *Th*. All solid surface boundaries were treated with boundary conditions of no leakage and no permeability. A zero pressure reference point for gauge pressure was assigned to the shell's left corner at bottom [49]. Additionally, the remaining shell walls were left untouched by any thermal flux.

2.4. Characteristic parameters

Melting volume fraction (MVF):

$$MVF = \frac{\iiint_V \varepsilon\phi dV}{\iiint_V \varepsilon dV} \tag{51}$$

where dV is the revolved volume element of the domain, and V is the revolved domain volume.

The stored energy is the sum of the apparent and latent heat as:

$$Q_{store} = Q_{latent} + Q_{sensible} \tag{52}$$

Where:

$$\begin{aligned} Q_{sensible} &= (\rho C_P)_{MF}(T-T_0)\oint_V (1-\varepsilon)dV \\ &+ \left[\oint_V \left(\int_{T_0}^{T} (\rho C_P)_{PCM}\varepsilon dT\right)dV\right] \\ &+ (\rho C_P)_{Wall} V_{Wall}(T-T_0) \end{aligned} \tag{53}$$

$$Q_{latent} = \oint_V \varepsilon L_{PCM}\rho_{PCM} f\, dV \tag{54}$$

where $(\rho C_P)_{PCM}$ as introduced in Eq (41) is a function of melt fraction (f) which is consequently a function of temperature according to Eq (21).

The following relationship computes the power of the energy storage

$$\text{Power} = Q_{store}/t \tag{55}$$

The average outlet velocity is computed by integrating the outlet velocity profile over the outlet surface as:

$$U_{HTF} = \iint_{HTF\ Outlet} w dA \tag{56}$$

and the average velocity is used to compute the HTF Reynolds number as:

$$Re = \rho_{HTF} \times 2 \times U_{HTF} \times \text{inside tube radius}/\eta_{HTF} \tag{57}$$

3. Numerical approach and model evaluation

3.1. Finite element method (FEM)

The computational fluid dynamics process was initially pursued through the application of the finite element method, converting the controlling equations into a more malleable weak form and integrating these over the relevant domains [55]. The fields of

Table 4
Details of selected domain discretization for mesh study.

Case	Mesh vertex	Quads	Triangles	Computational time (s)	
				Melting	Solidification
Normal	12245	6608	10710	1578	1065
Fine	22120	12894	17712	2927	2008
Finer	29654	15843	26747	4642	2914
Extra fine	**121574**	**56770**	**127725**	**23724**	**16992**
Extremely fine	382103	132132	496392	111692	71676

temperature and velocity were managed using second-order elements. Gauss quadrature integration was then invoked to apply these integrated equations across domain elements, thereby formulating a series of algebraic equations.

These resultant equations were processed iteratively and in a fully linked manner, utilizing the Newton method and the assistance of the concurrent PARDISO solver [56,57]. Implementing a Newton damping factor of 0.85 helped bolster the solver's stability and aid convergence. Phase change equations demonstrated sensitivity to time step increments, mainly due to the robust source terms within the momentum equations, which drive velocities to a null value within solidified areas.

Furthermore, the energy equation's latent heat phase change term strongly correlates with time. Therefore, to ensure time steps remain under control and maintain solution accuracy within a relative error under 10^{-4}, the backward differential formula (BDF) was used, with flexibility ranging from 1 to 2 [58]. This automatic time step management promises higher solution precision while concurrently diminishing the overall computation duration by choosing optimal and stable time steps.

3.2. Mesh examination

The mesh resolution can have a significant impact on the solution accuracy. In order to test the impact of mesh size on the accuracy of the results, a test case with the following parameters was selected. The geometrical parameters were adopted as follows: $H = 0.40$ m, HTF inside tube radius = 5/16" (7.9 mm), L = 6 × tube nominal radius, tube thickness = 0.049" (1.5 mm), nominal tube radius = 1/4" (6.4 mm), $L_{Fin} = L/2$, and $t_{Fin} = 4$ mm. The MF insert volume ratio was selected as $VR_{MF} = 0.1$, and the required power to compensate for the pressure drop in the HTF tube was fixed at 3 (mW); thus, the corresponding pressure drop was computed as 336 Pa. The operating conditions and thermophysical properties were explained in the modeling section. Five mesh sizes were adopted for the mesh study, and their details are reported in Table 4. The HTF region and tube walls have a structured geometry; hence, they were discretized by structured quad meshes. The rest of the domain, the fins, and the MF-PCM domain were discretized by triangular elements.

The simulations were executed for both the melting and solidification process, and the computational time for a full melting/solidification is reported in Table 2. The MVF during the phase change is plotted in Fig. 4. As can be seen, an increase in mesh size significantly increases the required computational time. An extra fine mesh with a total number of 184,495 demands 23724s computational time, while a normal mesh with 17318 elements requires only 1578s of computational time. Thus, increasing the mesh size by 10.65 times increases the computational time by 15 times for the melting process and about 16 times for the solidification process. Here, to keep the solution accuracy high, the mesh size of the extra fine was adopted for the rest of the simulations. A view of the adopted mesh and solution domain is illustrated in Fig. 5.

3.3. Model verification

The model correctness was verified by a comprehensive comparison between the results obtained in the current study and the empirical observations conducted by Zheng et al. [34] to assess the reliability and accuracy of the developed model and computations. The authors conducted a practical experiment focusing on the melting behavior of paraffin wax within a square enclosure filled with copper metal foam. The dimensions of the enclosure were set at 0.1 m in width and height. The paraffin wax was initially solid and maintained at a temperature of 14 °C. The left side of the enclosure was subjected to an electrical heater, generating a heat flux of 1150 W/m^2. This heat was stored by the MF and PCM within the cavity, causing a temperature rise until the PCM reached its phase transition point ($T_f = 55.3$ °C). The metal foam had a porosity of $\varepsilon = 0.95$, with a PPI (pores per inch) value of 5.

Fig. 6 portrays a detailed comparison between the simulation results obtained in this study and the empirical data [54]The agreement between the two sets of findings can be evaluated and validated by examining various aspects and parameters.

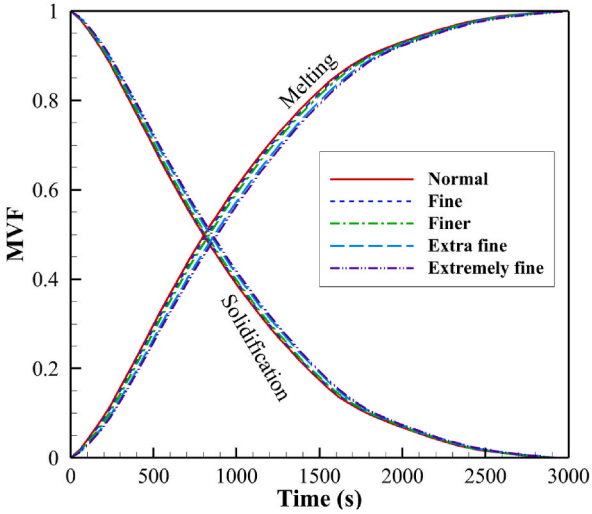

Fig. 4. MVF during the melting and solidification process for various meshes.

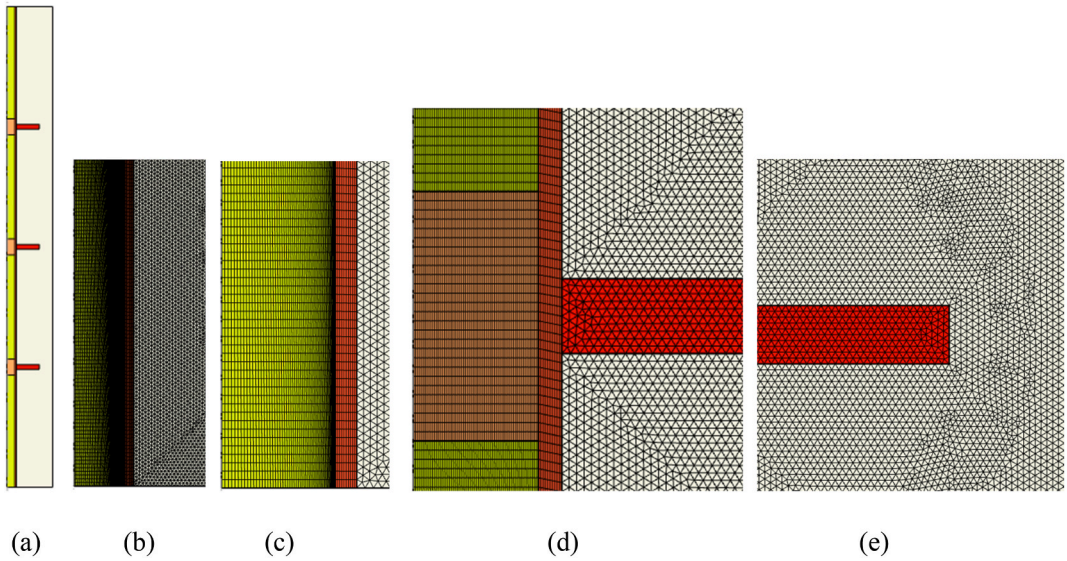

Fig. 5. A view of extra fine mesh adopted for computations. (a) An overview of the domain: the mesh elements are hidden since, due to very fine mesh, the image appears as pure black; (b) a zoomed view of mesh at the bottom left corner; (c) a zoomed view with more zoom at the bottom left corner; (d) a zoomed view at the first MF inserts, tube, and fin base; (e) a zoomed view inside the PCM-MF domain next to the end of a fin.

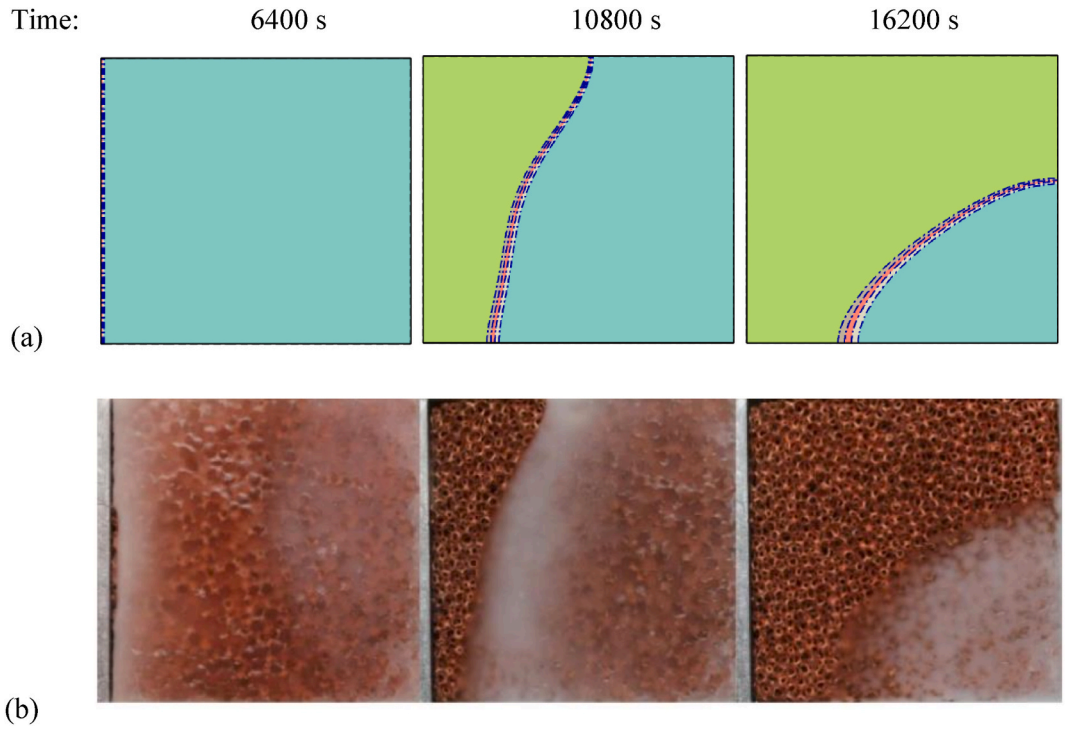

Fig. 6. Verifying the heat transfer phenomenon during the melting process within an enclosure filled with a composite material consisting of PCM-MF with a porosity of 0.95. The current simulations (a) were compared with (b) the experimental observations documented in Ref. [54] with permission from Elsevier.

Furthermore, the temperatures were monitored and recorded at the heated wall of the enclosure. Fig. 7 presents a comprehensive analysis, showcasing the temporal progression of the measured temperatures reported in Ref. [54], in comparison with the calculated temperatures derived from the current study. The results demonstrate a strong concurrence and consistency between the findings of this research and the empirical data [54], affirming the accuracy and validity of the current model and simulations.

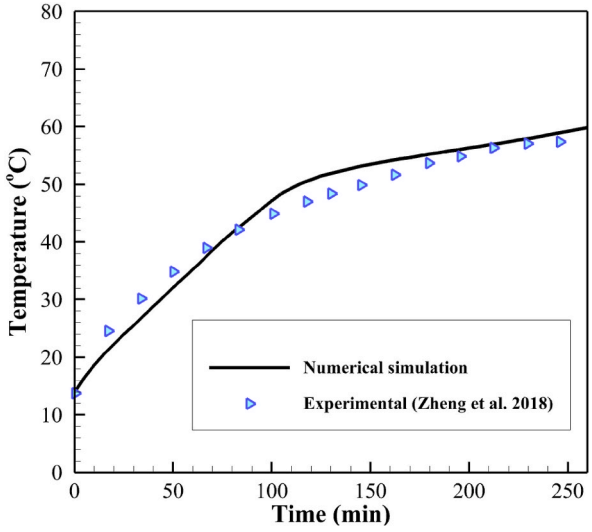

Fig. 7. Showcase of the temperature of the hot wall as observed in the melting process, as documented by Ref. [54], contrasted with the simulated outcomes attained through the current research endeavor.

4. Results and discussions

The impact of the length of the metal foam insert on the melting and solidification process has been addressed. The filled volume fraction ratio of the HTF ($0.05<VR_{MF}<0.70$) tube was considered as the control parameter. The same geometrical parameters as the mesh study were adopted. However, the length of MF inserts changes as VR_{MF} changes.

It is clear that the increase of VR_{MF} raises the amount of MF inserts inside the HTF tube and consequently increases the tube's flow resistance and drops the flow rate for constant inlet pressure. Fig. 8 (a) illustrates the relationship between the required pump power and the inlet pressure, while Fig. 8 (b) depicts the correlation between the flow rate and the inlet pressure. The dashed lines in Fig. 8 (a) represent two chosen cases of pumping powers: 3, 6, 9, and 12 (mW). The correlated inlet pressure can be deduced using the consistent pumping power lines. The inlet pressures corresponding to the chosen pumping powers are presented in Table 5.

The observations show that an increase in VR_{MF} results in a reduced flow rate and a heightened inlet pressure requirement. This can be attributed to the fact that a higher VR_{MF} means a larger portion of the HTF tube is occupied by the MF insert, thus posing a greater fluid flow resistance. Consequently, a higher pressure at the inlet becomes necessary to generate an increased flow rate. For larger VR_{MF} values, where the inlet pressure is high, the overall flow rate tends to decrease to sustain the constant pump power. Additionally, the corresponding Reynolds number of HTF flow for each case is detailed in Table 5. Besides, the computed time for 95 % melting, time for 95 % solidification, power at 95 % melting, and power at 95 % solidification are also reported in the table.

Starting with pump power, it is incremented in sets of 3(mW) from 3(mW) to 12(mW) for each batch of six cases. The pump power, being the primary source of energy in the system, has a significant effect on other variables. Increasing pump power results in higher inlet pressure and flow rate, meaning the pump can move more fluid through the system. For instance, when the pump power increased from 3(mW) (case 1) to 12(mW) (Case 19), inlet pressure and flow rate increased substantially from 256.4Pa to 11.7 mL^3/s to 594.4Pa and 20.2 mL^3/s respectively.

The volume ratio of the metal foam, VR_{MF}, also varies, starting from 0.05 and incrementing to 0.7 for each power setting. As the VR_{MF} increases, the flow rate generally decreases due to increased resistance to flow at a higher amount of MF. The Reynolds number is about 2000 or smaller for all cases, ensuring a laminar fluid flow in the HTF tube.

Their behavior does not exhibit a precise monotonic pattern regarding the melting and solidification times. Therefore, to better visualize the data, the results from Table 5 are presented graphically in Figs. 9 and 10, focusing on the two parameters: VR_{MF} and P_{Pump}. Fig. 11 illustrates the analysis of melting and solidification times, while Fig. 12 depicts the melting and solidification powers.

When utilizing MF inserts with a VR_{MF} value of 0.05, the solidification process takes approximately 34 min (Case 1) at a pumping power of 3 (mW). In contrast, employing a VRMF value of 0.25 necessitates around 39 min (Case 3) for the same pumping power. Consequently, employing only 5 % (VRMF = 0.05) MF inserts yields a substantial reduction of approximately 13 % in solidification time compared to a scenario utilizing 25 % ($VR_{MF}=0.25$) MF inserts.

Fig. 9 reveals that increasing the amount of inserted MF in the HTF tube, denoted as VR_{MF}, initially leads to longer melting and solidification until reaching a turning point at approximately $VR_{MF}=0.25$. Beyond this point, the melting and solidification times gradually decrease. For instance, at a pumping power of $P_{Pump}=6$ (mW), the melting time increases from 33 min in Case 7 ($VR_{MF}=0.05$) to 36 min in Case 9 ($VR_{MF}=0.25$) and then gradually decreases to 34 min in Case 12 ($VR_{MF}=0.7$). This trend is observed consistently across all pumping powers.

The fundamental cause is linked to the fluid flow rate in the HTF tube, which is constrained by the available pumping power. Two significant heat transfer mechanisms compete in the system: conduction heat transfer facilitated by the presence of MF inserts, which

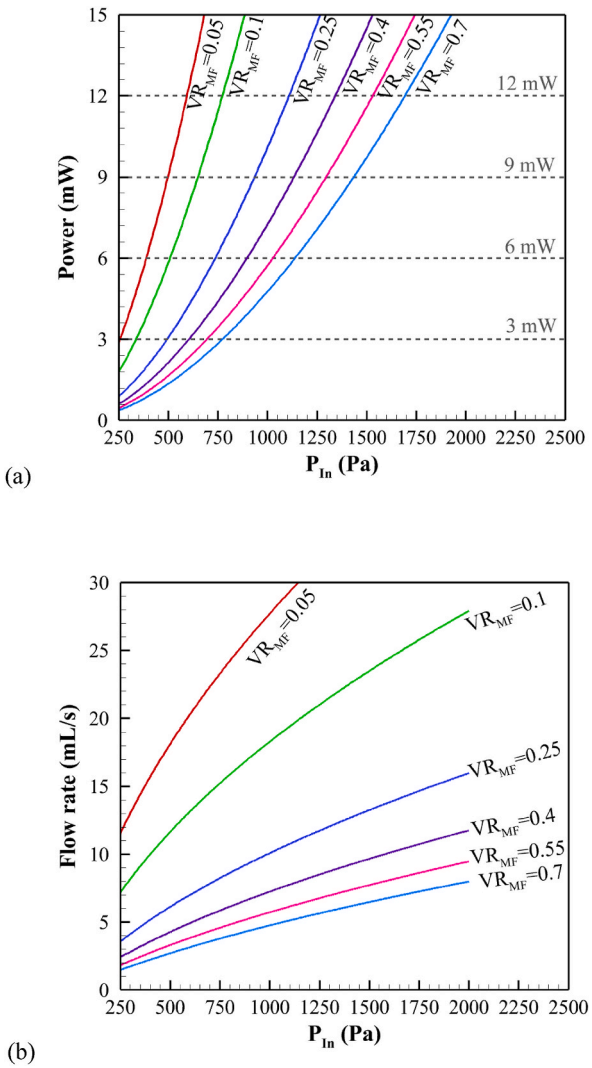

Fig. 8. Illustrates the effect of inlet HTF (heat transfer fluid) pressure on (a) pump power and (b) the corresponding flow rate. These graphs are crucial for analyzing the hydrodynamic behavior of HTF within the tube. The dashed lines in the pump power graph indicate the levels of constant pumping power examined in this study. The horizontal axis represents the inlet pressure, correlating the flow rate and pump power for each percentage of metal foam (MF) insert filling.

enhances the effective thermal conductivity and directs heat transfer from the HTF side to the MF-PCM domain, and convection heat transfer weakened by the reduced flow rate in the HTF side due to the presence of MF inserts. The reduction in flow rate diminishes convection heat transfer, resulting in decreased heat transfer from the HTF side to the MF-PCM side. Therefore, Fig. 9 displays local turning points in the graphs where each mechanism provides favorable heat transfer effects.

The melting and solidification powers exhibit a maximum at a low volume of metal inserts ($VR_{MF} = 0.05$) and a high volume of metal inserts ($VR_{MF} = 0.7$), with a decline in power between these values. This behavior is influenced by the observed charging and discharging times in Fig. 11, which follow a similar physical trend.

For instance, in the 3(mW) power group, power at 95 % melting shows a decrease from 159.91W (Case 1) to 144.52W (Case 4) as VR_{MF} increases and then a subsequent increase as VR_{MF} continues to rise, for instance, its increases to 148.90 W for case 7 ($VR_{MF} = 0.7$). This could suggest an optimal VR_{MF} for energy efficiency during the melting process.

Fig. 11 presents the melting and solidification time history for the optimal cases ($VR_{MF} = 0.05$ and $VR_{MF} = 0.7$) and the worst case ($VR_{MF} = 0.25$), selected based on the observed trends in Figs. 9 and 10. The results are plotted for various pumping powers and show that the increase in the pumping power leads to an accelerated phase change process, primarily due to enhanced convective heat transfer in the HTF tube. The curves also highlight a noticeable distinction between a low pumping power of 3 (mW) and a higher power of $P_{pump} \geq 6$ (mW). A further increase in pumping power improves the heat transfer rate slightly. Furthermore, increasing the pumping power can be highly advantageous in the case of $VR_{MF} = 0.7$, as the flow rate is already low due to the high resistance caused by a significant amount of MF inserts, and there is still room for further enhancement of convective heat transfer. On the other hand, the potential for improvement through increased pumping power is minimal for the low volume of MF insert ($VR_{MF} = 0.05$).

Table 5
List of VR_{MF}, corresponding computed inlet pressures for fixed pump powers, and the melting and solidification times.

Case	Control parameters		Computed HTF flow characteristics			Computed heat transfer characteristics			
	Pump power (mW)	VR_{MF}	Inlet pressure (Pa)	Flow rate (mL^3/s)	Re	Time for 95 % melting (min)	Time for 95 % solidification (min)	Power at 95 % melting (W)	Power at 95 % solidification (W)
1	3	0.05	256.4	11.7	1159.7	35	34	159.91	155.94
2	3	0.1	337.6	8.9	880.6	37	38	152.78	143.19
3	3	0.25	493.9	6.1	602	39	39	145.16	142.29
4	3	0.4	604.3	5	492	39	38	144.52	146.24
5	3	0.55	694.6	4.3	428.1	39	38	146.48	147.24
6	3	0.7	772.6	3.9	384.8	38	38	148.90	147.56
7	6	0.05	389	15.4	1528.5	33	32	169.87	169.39
8	6	0.1	508.9	11.8	1168.4	34	34	163.48	163.05
9	6	0.25	737	8.1	806.9	36	35	157.60	156.32
10	6	0.4	896.8	6.7	663	36	35	158.70	157.28
11	6	0.55	1026.9	5.8	579.1	35	34	162.79	162.28
12	6	0.7	1139.1	5.3	522	34	33	168.14	166.60
13	9	0.05	498.1	18.1	1790.6	32	31	175.39	175.56
14	9	0.1	649.3	13.9	1373.7	35	34	161.38	160.64
15	9	0.25	934.9	9.6	954	34	34	164.31	163.02
16	9	0.4	1134.1	7.9	786.5	34	34	166.25	165.49
17	9	0.55	1295.7	6.9	688.4	33	33	170.39	169.70
18	9	0.7	1435	6.3	621.6	32	31	178.02	177.59
19	12	0.05	594.4	20.2	2000.6	31	30	179.17	179.39
20	12	0.1	773	15.5	1538.6	32	32	173.30	173.29
21	12	0.25	1108.7	10.8	1072.7	33	33	168.86	168.66
22	12	0.4	1341.9	8.9	886.2	33	32	171.33	171.65
23	12	0.55	1530.7	7.8	776.9	32	31	177.13	176.87
24	12	0.7	1693.3	7.1	702.3	31	30	184.51	184.28

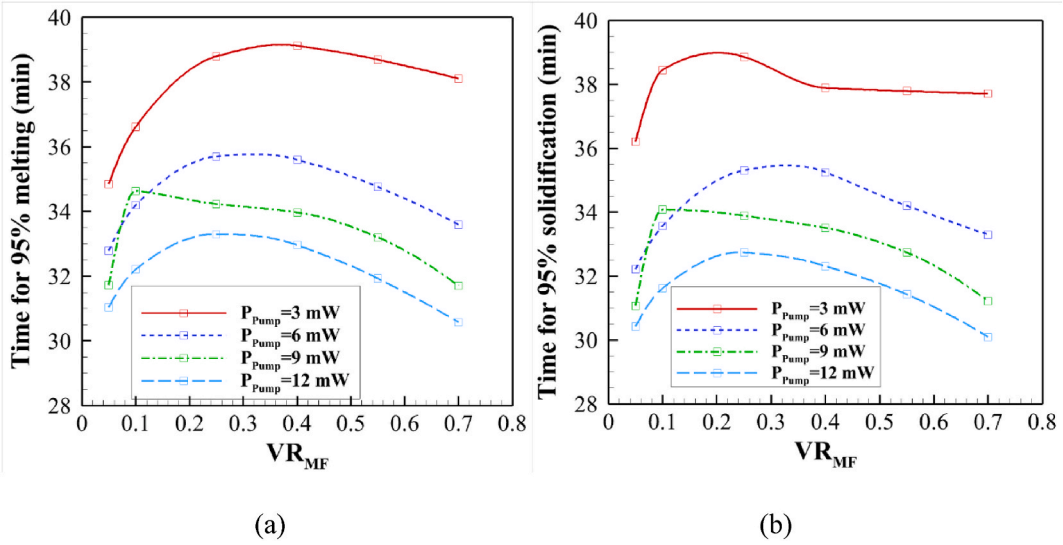

Fig. 9. The effects of VR_{MF} and P_{pump} (pumping power) on (a) the melting time (95 % melt, i.e., MVF = 0.95), and (b) the solidification time (95 % solidification, i.e., MVF = 0.05).

The graphical representations in Figs. 12 and 13 offer detailed insight into the phase change interface, streamlines, velocity contours, and temperature fields for the melting and solidification processes. Fig. 12 explicitly illustrates the outcomes obtained for Case 19, representing an exemplary design. In contrast, Fig. 13 showcases the results corresponding to Case 21, which can be classified as the least favorable scenario, with a fixed pumping power of $P_{pump} = 12$ (mW).

During the melting process, as shown in Fig. 12, the melting initiates at the tube wall and gradually progresses toward the inner region of the domain. The fins play a crucial role in rapidly melting the PCM around them. As a result, in the early times of the 300s, the area surrounding the fins was entirely molten. Subsequently, the melting interface advances towards the right tube at $t = 600$s and $t = 1200$s. By the 1800s, most of the PCM domain had transformed into a molten state, with only small regions remaining solid in the top and bottom right corners. Examining the velocity magnitudes reveals that the solid regions exhibit zero velocities, while the molten

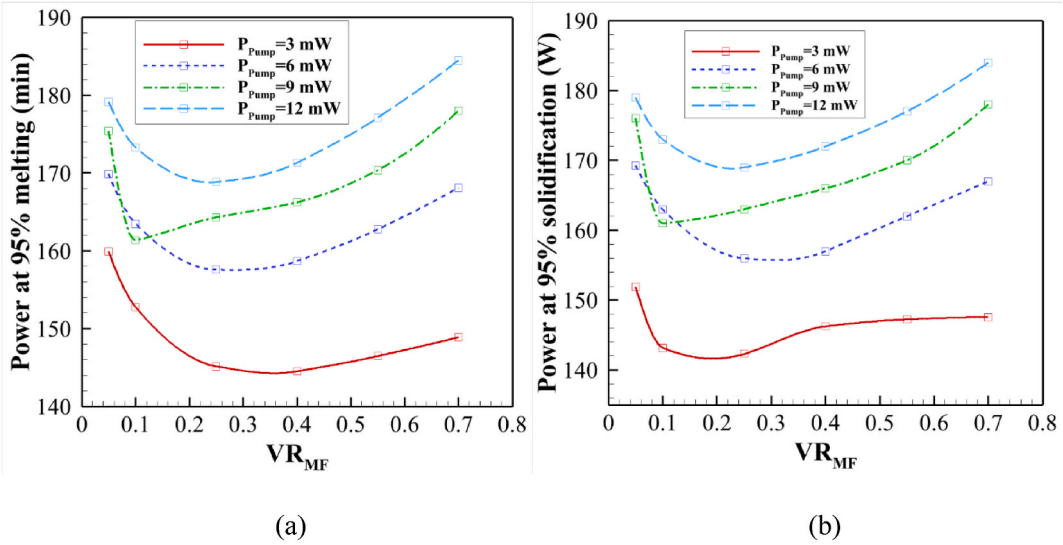

Fig. 10. The impact of VR_{MF} and P_{pump} on (a) the melting power (95 % melt, *i.e.*, MVF = 0.95), and (b) the solidification power (95 % solidification, i.e., MVF = 0.05).

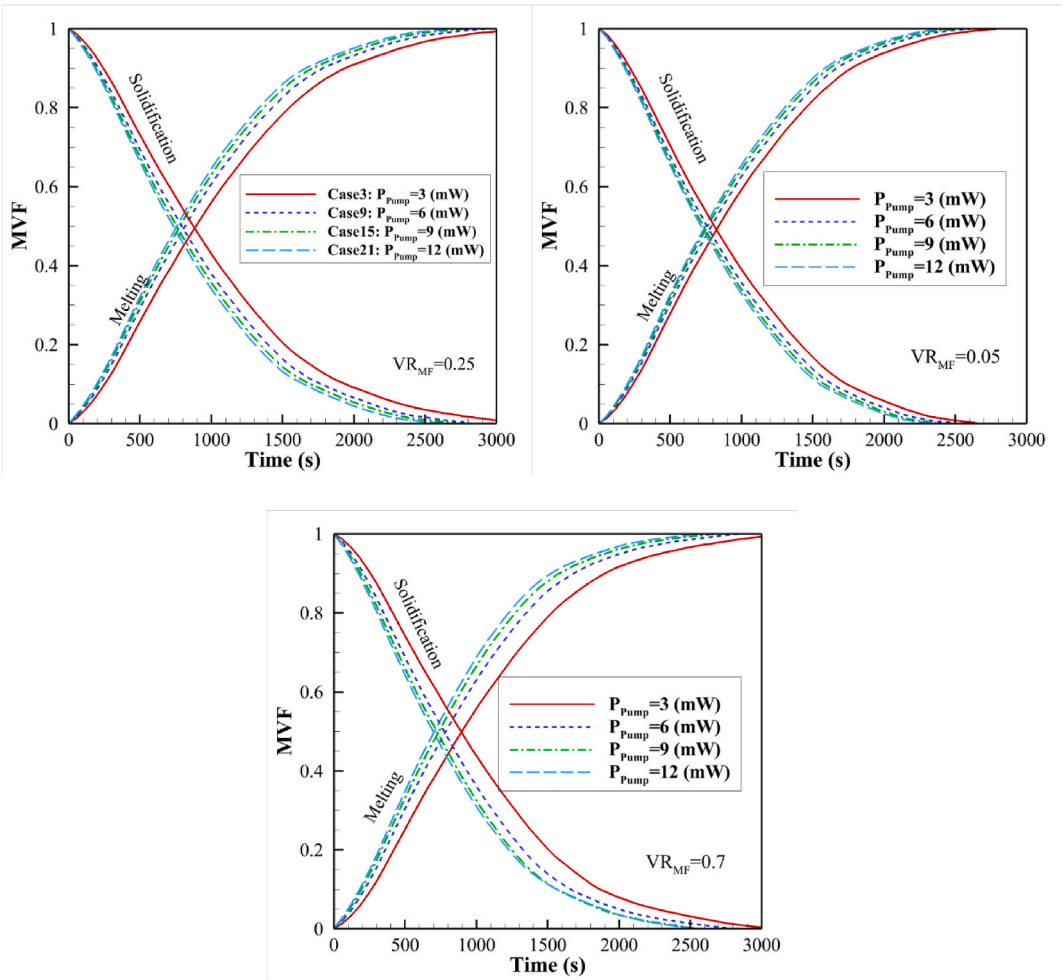

Fig. 11. Impact of metal foam volume ratio (VR_{MF}) on the MVF during the melting and solidification process.

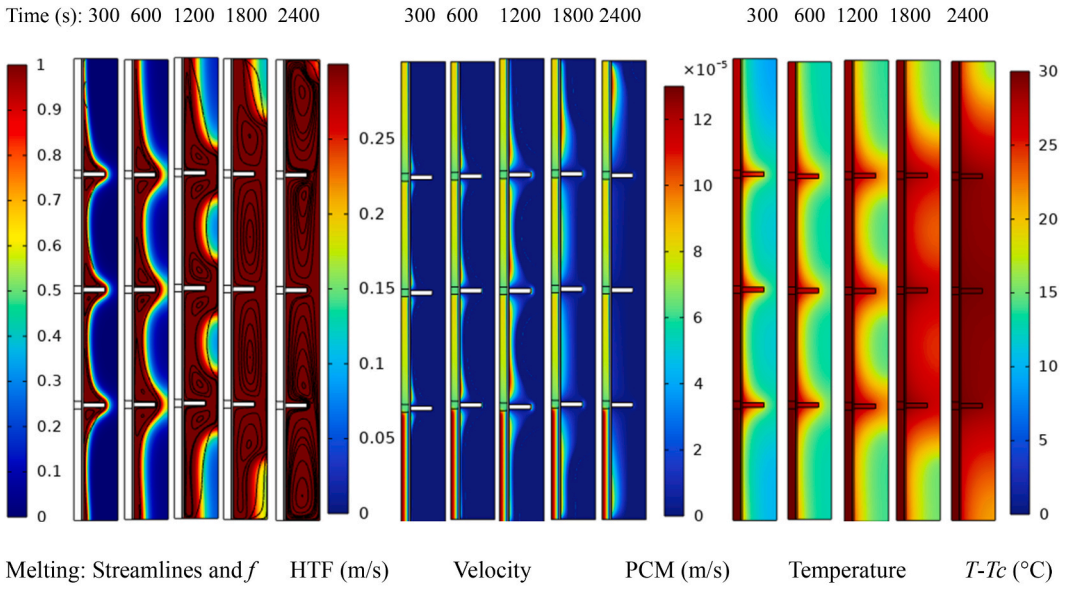

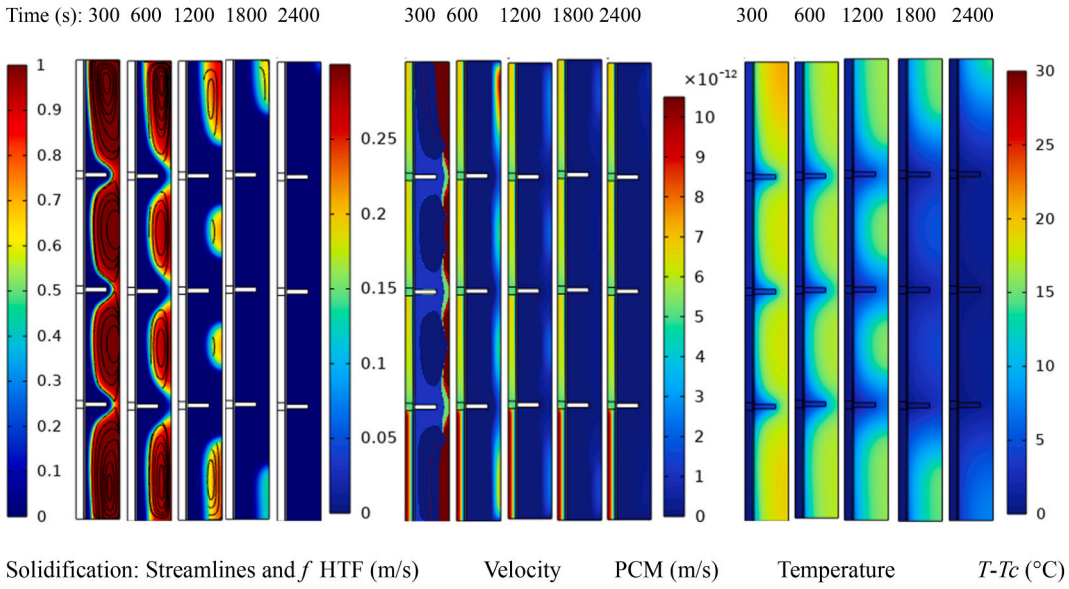

Fig. 12. A comprehensive visualization of the phase change process for Case 19 with $P_{\text{Pump}} = 12$ (mW) and $VR_{\text{MF}} = 0.05$ during the melting and solidification, showcasing an exemplary design. The temperature is reported in the temperature difference between the lowest temperature (Tc) and the field temperature T in the form of T-Tc.

regions adjacent to the tube wall experience relatively low velocities. This observation aligns with the notable temperature gradients and most heat transfer occurring in these regions.

The streamlines, consistent with the velocity maps, illustrate local circulations between the fins. Isotherm plots highlight hot spots in the fins at all stages of heat transfer, indicating effective heat transfer from the HTF side to the fins. This effectiveness is attributed to MF inserts, which facilitate heat channeling from the HTF fluid toward the base of the fins. Analyzing the velocities on the HTF side reveals that the MF inserts contribute to achieving uniform velocities across most sections of the HTF tube. A uniform velocity profile significantly enhances convection heat transfer over tube walls, surpassing the capabilities of a velocity profile characterized by a boundary layer shape. Consequently, the MF inserts prove to be advantageous from this perspective.

Upon examining the solidification images, it becomes evident that the solidification process follows a pattern reverse to that of melting. Solidification initiates at the tube wall and around the fins, gradually progressing toward the PCM domain. A fundamental difference arises in flow circulations and streamlines, occurring inside the domain while the regions around the fins solidify. This distinction establishes a significant disparity in free convection between the melting and solidification processes. Examining the

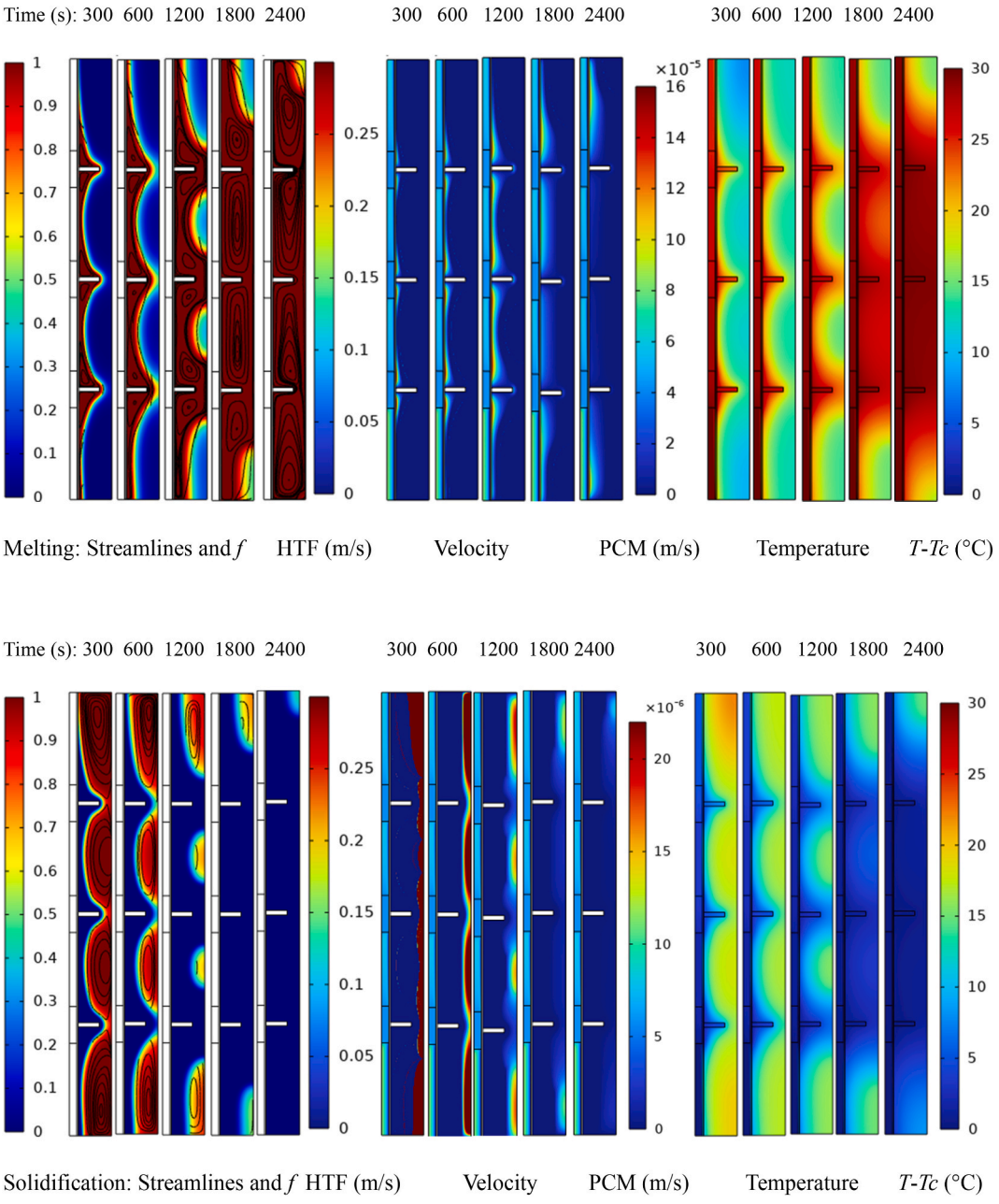

Fig. 13. The outcomes for Case 21 illustrate the least favorable scenario under $P_{Pump} = 12$ (mW) and $VR_{MF} = 0.25$ during the melting and solidification. The temperature is reported in the temperature difference between the lowest temperature (Tc) and the field temperature T in the form of T-Tc.

velocities during solidification indicates their significance primarily in the early stages, where significant temperature gradients and ample molten PCM in the right regions of the PCM domain facilitate significant velocities. As solidification progresses, layers of solidified PCM form over the HTF tube and fins, acting as insulating barriers that impede heat transfer flow.

Additionally, the availability of molten PCM, essential for natural convection, diminishes. Consequently, the strength of natural convection flows notably reduces as solidification progresses. Temperature profiles at the early stages of solidification ($t = 300$s) reveal a few mid-temperature spots in the fins, indicating that heat transfer from the PCM domain is comparable to heat transfer at the HTF side. However, as solidification advances, free convection and conduction mechanisms weaken, causing the fins' temperature to approach that of the HTF fluid. This leads to a decrease in the significance of heat transfer enhancement at the HTF side. As a result, the solidification profiles, as depicted in Fig. 13, become nearly identical during the final stages of the solidification process,

Fig. 13 exhibits a similar trend to the results shown in Fig. 12. However, there are differences in melting interface locations and the strength of convection heat transfer flows. Examining the temperature maps in Fig. 13 during melting reveals yellow spots in the early

stages, indicating that heat transfer mechanisms at the HTF side are not as strong as those observed in Case 19. This low heat transfer can be attributed to a small HTF fluid flow rate caused by the MF insert's high resistance, despite a constant pumping power. By the 1800s, the fins reach a temperature similar to that of the HTF fluid, highlighting the dominant effect of heat transfer at the HTF side. At this stage, MF inserts and heat transfer at the HTF side become less critical. The solidification process in Case 21 exhibits similar features to those observed in Case 19. However, due to the weaker heat transfer rate at the HTF side, the natural convection effects and velocities within the PCM domain are also reduced.

5. Conclusions

The phase transition heat transfer during the melting and solidification processes of PCMs in a shell-tube thermal energy storage unit was the subject of this investigation. The research focused on enhancing heat transfer on the HTF side by placing MF inserts within the HTF tube. Moreover, heat transfer on the PCM side was augmented by a combination of MFs and fins. To accurately model the transient heat transfer in the MF domains, a two-temperature local thermal non-equilibrium model was applied, and the FEM was utilized to solve the governing equations for fluid flow and heat transfer. The key findings of the research can be summarized as follows:

The results underscore a critical balance between the volume of MF and the system's overall performance. Introducing a mere 5 % MF volume notably improved phase transition efficiency, cutting solidification times by approximately 13 % compared to systems with a 25 % MF volume. This finding demonstrates that even a small, well-engineered MF configuration can notably decrease phase transition times, thereby improving energy storage capability and efficiency.

Furthermore, the study explored how the length of MF inserts within the HTF tube affects system performance, with a specific focus on the filled volume fraction ratio as a key control parameter. An increase in this ratio was found to lower the flow rate, caused by increased resistance within the tube. This, in turn, required a higher inlet pressure to achieve adequate flow rates.

A distinct trend emerged in relation to the quantity of MF utilized: as the MF volume increased, it initially resulted in longer melting and solidification durations until hitting a critical volume fraction ratio of 0.25. After surpassing this threshold, these durations began to shorten, closely linked to the fluid flow rate constrained by the accessible pumping power.

Additionally, the analysis revealed a particular pattern in melting and solidification powers, which peaked at both low and high volumes of metal inserts. The decline in power between these extremes aligns with the trends seen in charging and discharging times, highlighting the complex interplay between the volume of metal foam, flow resistance, and thermal efficiency.

The practical implementation of these findings in building applications offers significant potential for enhancing thermal management. By optimizing the placement and volume of MF inserts within the HTF tubes of shell-tube thermal energy storage units, buildings can achieve more efficient heat storage, reducing energy consumption and increasing overall sustainability in heating and cooling systems.

CRediT authorship contribution statement

Fathi Alimi: Investigation, Funding acquisition, Formal analysis, Data curation, Conceptualization. **Hakim S. Sultan Aljibori:** Resources, Methodology, Investigation, Conceptualization. **Mohamed Bouzidi:** Writing – review & editing, Writing – original draft, Project administration, Formal analysis, Conceptualization. **Aeshah Alasmari:** Writing – original draft, Resources, Methodology, Investigation, Funding acquisition, Formal analysis. **Shima Yazdani:** Writing – original draft, Visualization, Validation, Software, Formal analysis. **Mehdi Ghalambaz:** Writing – review & editing, Writing – original draft, Resources, Project administration.

Declaration of competing interest

The authors clarify that there is no conflict of interest for report.

Data availability

Data will be made available on request.

Acknowledgments

The authors are thankful to the Deanship of Graduate Studies and Scientific Research at University of Bisha for supporting this work through the Fast-Track Research Support Program.

References

[1] M.H. Albadi, E.F. El-Saadany, Demand response in electricity markets: an overview. 2007 IEEE Power Engineering Society General Meeting, 2007, pp. 1–5. IEEE.
[2] D. Jayathunga, H. Karunathilake, M. Narayana, S. Witharana, Phase change material (PCM) candidates for latent heat thermal energy storage (LHTES) in concentrated solar power (CSP) based thermal applications-A review, Renew. Sustain. Energy Rev. 189 (2024) 113904.
[3] M. Ghalambaz, M. Sheremet, M.A. Fauzi, M. Fteiti, O. Younis, A scientometrics review of solar thermal energy storage (STES) during the past forty years, J. Energy Storage 66 (2023) 107266.
[4] M. Fang, X. Zhang, Y. Liu, S. Cai, Recent advances in photovoltaic and photovoltaic thermal technologies of integrated phase-change materials: a review, Sol. RRL 8 (8) (2024) 2400033.

[5] A. Mourad, A. Aissa, Z. Said, O. Younis, M. Iqbal, A. Alazzam, Recent advances on the applications of phase change materials for solar collectors, practical limitations, and challenges: a critical review, J. Energy Storage 49 (2022) 104186.
[6] S. Tian, J. Ma, S. Shao, Q. Tian, Z. Wang, Y. Zhao, B. Tan, Z. Zhang, Z. Sun, Estimation of heat transfer performance of latent thermal energy storage devices with different heat transfer interface types: a review, J. Energy Storage 86 (2024) 111315.
[7] Y. Gao, F. He, T. Xu, X. Meng, M. Zhang, L. Yan, W. Gao, Thermal performance analysis of sensible and latent heat thermal energy storage tanks: a contrastive experiment, J. Build. Eng. 32 (2020) 101713.
[8] A. Saxena, E. Cuce, D.B. Singh, M. Sethi, P.M. Cuce, A.A. Sagade, A. Kumar, Experimental studies of latent heat storage based solar air heater for space heating: a comparative analysis, J. Build. Eng. 69 (2023) 106282.
[9] K.H. Almitani, N.H. Abu-Hamdeh, A.M. Abusorrah, H.A. AL-bonsrulah, A. Abd Elmotaleb, Simulation of latent heat thermal storage evaluation utilizing NEPCM for new ventilation system for building, J. Build. Eng. 76 (2023) 107288.
[10] X. Jin, S. You, G. Huang, A.C. Lai, Techno-economic assessment of the solar-assisted heat pump latent heat thermal energy storage system for water heating, Energy Build. 301 (2023) 113657.
[11] W. Wu, J. Chen, X. Kang, Numerical simulations on the thermal performance of ventilated walls with passive solar heating and latent heat storage in winter, Energy Build. 299 (2023) 113626.
[12] C. Cárdenas-Ramírez, M.A. Gómez, F. Jaramillo, A.F. Cardona, A.G. Fernández, L.F. Cabeza, Experimental steady-state and transient thermal performance of materials for thermal energy storage in building applications: from powder SS-PCMs to SS-PCM-based acrylic plaster, Energy 250 (2022) 123768.
[13] H.A. Al-Salami, N.S. Dhaidan, H.H. Abbas, F.N. Al-Mousawi, R.Z. Homod, Review of PCM charging in latent heat thermal energy storage systems with fins, Therm. Sci. Eng. Prog. (2024) 102640.
[14] S. Seddegh, X. Wang, M.M. Joybari, F. Haghighat, Investigation of the effect of geometric and operating parameters on thermal behavior of vertical shell-and-tube latent heat energy storage systems, Energy 137 (2017) 69–82.
[15] D.I. Berrocal, J. Blandon Rodriguez, M.D.L.A. Ortega Del Rosario, I. Harris, A.M. James Rivas, Heat transfer enhancements assessment in hot water generation with phase change materials (PCMs): a review, Energies 17 (10) (2024) 2350.
[16] M.A. Said, H. Togun, A.M. Abed, N. Biswas, H.I. Mohammed, H.S. Sultan, J.M. Mahdi, P. Talebizadehsardari, Evaluation of wavy wall configurations for accelerated heat recovery in triplex-tube energy storage units for building heating applications, J. Build. Eng. (2024) 109762.
[17] N.B. Khedher, H. Togun, A.M. Abed, H.M.T. Al-Najjar, A. Dulaimi, H.I. Mohammed, J.M. Mahdi, A. Yvaz, P. Talebizadehsardari, Discharge performance assessment of a vertical double-pipe latent heat storage unit equipped with circular Y-shaped fins, J. Build. Eng. (2023) 106870.
[18] N.B. Khedher, H. Togun, A.M. Abed, H.I. Mohammed, J.M. Mahdi, R.K. Ibrahem, W. Yaïci, P. Talebizadehsardari, A. Keshmiri, Comprehensive analysis of melting enhancement by circular Y-shaped fins in a vertical shell-and-tube heat storage system, Eng. Appli. Computation. Fluid Mech. 17 (1) (2023) 2227682.
[19] M. Eisapour, A.H. Eisapour, A. Shafaghat, H.I. Mohammed, P. Talebizadehsardari, Z. Chen, Solidification of a nano-enhanced phase change material (NePCM) in a double elliptical latent heat storage unit with wavy inner tubes, Sol. Energy 241 (2022) 39–53.
[20] J.M. Mahdi, H.I. Mohammed, E.T. Hashim, P. Talebizadehsardari, E.C. Nsofor, Solidification enhancement with multiple PCMs, cascaded metal foam and nanoparticles in the shell-and-tube energy storage system, Appl. Energy 257 (2020) 113993.
[21] H.M.T. Al-Najjar, J.M. Mahdi, D.O. Bokov, N.B. Khedher, N.K. Alshammari, M.J. Catalan Opulencia, M.A. Fagiry, W. Yaïci, P. Talebizadehsardari, Improving the melting duration of a PV/PCM system integrated with different metal foam configurations for thermal energy management, Nanomaterials 12 (3) (2022) 423.
[22] E. Hamidi, P. Ganesan, R. Sharma, K. Yong, Computational study of heat transfer enhancement using porous foams with phase change materials: a comparative review, Renew. Sustain. Energy Rev. 176 (2023) 113196.
[23] M. Boujelbene, J.M. Mahdi, H.S. Sultan, R.Z. Homod, A. Yvaz, I.S. Chatroudi, P. Talebizadehsardari, The potential of arc-shaped fins for expedited solidification in triplex-tube latent heat storage: parametric investigation, J. Build. Eng. 82 (2024) 108176.
[24] M. Boujelbene, J.M. Mahdi, A.M. Abed, M.S. Ghanim, K.A. Hammoodi, H.I. Mohammed, H. Togun, P. Talebizadehsardari, The potential of arch-shaped fins for energy-charge enhancement in triplex-tube heat storage: comparative analysis and optimization, J. Energy Storage 79 (2024) 110188.
[25] M. Ghalambaz, S. Mehryan, A. Hajjar, M.A. Fteiti, O. Younis, P.T. Sardari, W. Yaïci, Latent heat thermal storage in non-uniform metal foam filled with nano-enhanced phase change material, Sustainability 13 (4) (2021) 2401.
[26] C.-C. Chueh, S.-C. Hung, Numerical investigation of melting of a phase-change material in H-type shell tubes, Appl. Therm. Eng. 236 (2024) 121470.
[27] A. Pizzolato, A. Sharma, K. Maute, A. Sciacovelli, V. Verda, Design of effective fins for fast PCM melting and solidification in shell-and-tube latent heat thermal energy storage through topology optimization, Appl. Energy 208 (2017) 210–227.
[28] S. Kuboth, A. König-Haagen, D. Brüggemann, Numerical analysis of shell-and-tube type latent thermal energy storage performance with different arrangements of circular fins, Energies 10 (3) (2017) 274.
[29] X. Li, S. Chen, Y. Tan, G. Tian, Z. Wang, S. Tang, L. Wang, Thermal storage performance of a novel shell-and-tube latent heat storage system: active role of inner tube improvement and fin distribution optimization, Renew. Energy (2024) 120695.
[30] H. Li, C. Hu, D. Tang, Z. Rao, Improving heat storage performance of shell-and-tube unit by using structural-optimized spiral fins, J. Energy Storage 79 (2024) 110212.
[31] Y. Lu, M. Wu, H. Zuo, H. Xu, K. Zeng, B. Chi, J. Gao, Z. Fang, H. Yang, H. Chen, Melting enhancement in a shell-and-tube latent heat storage unit with staggered fin-foam synergistic configuration, J. Energy Storage 82 (2024) 110505.
[32] C. Wang, E. Meng, J. Zhao, B. Zhou, J. Li, Study on the thermal performance of a new type of latent heat storage unit (LHSU), J. Build. Eng. 64 (2023) 105630.
[33] F. Şimşek, H. Demirci, Investigation of the use of new fin on the melting time of the phase change material stored in the heat exchanger by computational fluid dynamics analysis, J. Build. Eng. 91 (2024) 109505.
[34] M. Boujelbene, H.I. Mohammed, H.S. Sultan, M. Eisapour, Z. Chen, J.M. Mahdi, A. Cairns, P. Talebizadehsardari, A comparative study of twisted and straight fins in enhancing the melting and solidifying rates of PCM in horizontal double-tube heat exchangers, Int. Commun. Heat Mass Tran. 151 (2024) 107224.
[35] P.T. Sardari, R. Babaei-Mahani, D. Giddings, S. Yasseri, M. Moghimi, H. Bahai, Energy recovery from domestic radiators using a compact composite metal Foam/PCM latent heat storage, J. Clean. Prod. 257 (2020) 120504.
[36] M. Ghalambaz, M. Aljaghtham, A.J. Chamkha, A. Abdullah, A. Alshehri, M. Ghalambaz, Anisotropic metal foam design for improved latent heat thermal energy storage in a tilted enclosure, Int. J. Mech. Sci. 238 (2023) 107830.
[37] Y. Shen, S. Liu, A.R. Mazhar, J. Wang, Y. Li, Phase change materials embedded with tuned porous media to alleviate overcharging problem of cascaded latent heat storage system for building heating, Energy Build. 281 (2023) 112746.
[38] J. Wołoszyn, K. Szopa, A combined heat transfer enhancement technique for shell-and-tube latent heat thermal energy storage, Renew. Energy 202 (2023) 1342–1356.
[39] J. Guo, Z. Liu, Z. Du, J. Yu, X. Yang, J. Yan, Effect of fin-metal foam structure on thermal energy storage: an experimental study, Renew. Energy 172 (2021) 57–70.
[40] M. Bouzidi, M. Sheremet, K. Shank, S. Tiari, M. Ghalambaz, Charging and discharging heat transfer improvement of shell-tube storage utilizing a partial layer of anisotropic metal foam, J. Energy Storage 79 (2024) 109948.
[41] S. Zhang, Y. Yao, Y. Jin, Z. Shang, Y. Yan, Heat transfer characteristics of ceramic foam/molten salt composite phase change material (CPCM) for medium-temperature thermal energy storage, Int. J. Heat Mass Tran. 196 (2022) 123262.
[42] Y. Yao, H. Wu, Interfacial heat transfer in metal foam porous media (MFPM) under steady thermal conduction condition and extension of Lemlich foam conductivity theory, Int. J. Heat Mass Tran. 169 (2021) 120974.
[43] Y. Yao, H. Wu, Macroscale modeling of solid–liquid phase change in metal foam/paraffin composite: effects of paraffin density treatment, thermal dispersion, and interstitial heat transfer, J. Therm. Sci. Eng. Appl. 13 (4) (2021).
[44] Y. Yao, H. Wu, Z. Liu, Direct simulation of interstitial heat transfer coefficient between paraffin and high porosity open-cell metal foam, J. Heat Tran. 140 (3) (2018).

[45] X. Yang, P. Wei, X. Wang, Y.-L. He, Gradient design of pore parameters on the melting process in a thermal energy storage unit filled with open-cell metal foam, Appl. Energy 268 (2020) 115019.
[46] V. Joshi, M.K. Rathod, Thermal transport augmentation in latent heat thermal energy storage system by partially filled metal foam: a novel configuration, J. Energy Storage 22 (2019) 270–282.
[47] V.V. Calmidi, R.L. Mahajan, Forced convection in high porosity metal foams, J. Heat Tran. 122 (3) (2000) 557–565.
[48] Z. Liu, Y. Yao, H. Wu, Numerical modeling for solid–liquid phase change phenomena in porous media: shell-and-tube type latent heat thermal energy storage, Appl. Energy 112 (2013) 1222–1232.
[49] J. Shafi, M. Ghalambaz, M. Fteiti, M. Ismael, M. Ghalambaz, Computational modeling of latent heat thermal energy storage in a shell-tube unit: using neural networks and anisotropic metal foam, Mathematics 10 (24) (2022) 4774.
[50] A.I.N. Korti, H. Guellil, Experimental study of the effect of inclination angle on the paraffin melting process in a square cavity, J. Energy Storage 32 (2020) 101726.
[51] A. Agarwal, R. Sarviya, Characterization of commercial grade paraffin wax as latent heat storage material for solar dryers, Mater. Today: Proc. 4 (2) (2017) 779–789.
[52] N. Ukrainczyk, S. Kurajica, J. Šipušić, Thermophysical comparison of five commercial paraffin waxes as latent heat storage materials, Chem. Biochem. Eng. Q. 24 (2) (2010) 129–137.
[53] S.-K. Choi, S.-O. Kim, T.-H. Lee, Dohee-Hahn, Computation of the natural convection of nanofluid in a square cavity with homogeneous and nonhomogeneous models, Numer. Heat Tran., Part A: Applications 65 (4) (2014) 287–301.
[54] H. Zheng, C. Wang, Q. Liu, Z. Tian, X. Fan, Thermal performance of copper foam/paraffin composite phase change material, Energy Convers. Manag. 157 (2018) 372–381.
[55] O.C. Zienkiewicz, R.L. Taylor, P. Nithiarasu, The Finite Element Method for Fluid Dynamics, seventh ed., Butterworth-Heinemann, Oxford, 2014.
[56] M. Bollhöfer, O. Schenk, R. Janalik, S. Hamm, K. Gullapalli, State-of-the-art sparse direct solvers, in: Parallel Algorithms in Computational Science and Engineering, Springer, 2020, pp. 3–33.
[57] M. Bollhöfer, A. Eftekhari, S. Scheidegger, O. Schenk, Large-scale sparse inverse covariance matrix estimation, SIAM J. Sci. Comput. 41 (1) (2019) A380–A401.
[58] G. Söderlind, L. Wang, Adaptive time-stepping and computational stability, J. Comput. Appl. Math. 185 (2) (2006) 225–243.